Virologica Sinica 38 (2023) 531–540

Contents lists available at ScienceDirect

Virologica Sinica

journal homepage: www.keaipublishing.com/en/journals/virologica-sinica
www.virosin.org

Research Article

Unusual substructure conformations observed in crystal structures of a dicistrovirus RNA-dependent RNA polymerase suggest contribution of the N-terminal extension in proper folding

Xiang Fang [a,c], Guoliang Lu [a], Yanchun Deng [b], Sa Yang [d], Chunsheng Hou [b,*], Peng Gong [a,c,e,*]

[a] Key Laboratory of Special Pathogens and Biosafety, Wuhan Institute of Virology, Chinese Academy of Sciences, Wuhan, 430207, China
[b] Institute of Bast Fiber Crops, Chinese Academy of Agricultural Sciences, Changsha, 410205, China
[c] University of Chinese Academy of Sciences, Beijing, 100049, China
[d] Institute of Apicultural Research, Chinese Academy of Agricultural Sciences, Beijing, 100193, China
[e] Hubei Jiangxia Laboratory, Wuhan, 430207, China

ARTICLE INFO

Keywords:
Israeli acute paralysis virus (IAPV)
Poliovirus
RNA-dependent RNA polymerase (RdRP)
Crystal structure
Catalytic motif

ABSTRACT

The *Dicistroviridae* is a virus family that includes many insect pathogens. These viruses contain a positive-sense RNA genome that is replicated by the virally encoded RNA-dependent RNA polymerase (RdRP) also named $3D^{pol}$. Compared with the *Picornaviridae* RdRPs such as poliovirus (PV) $3D^{pol}$, the *Dicistroviridae* representative Israeli acute paralysis virus (IAPV) $3D^{pol}$ has an additional N-terminal extension (NE) region that is about 40-residue in length. To date, both the structure and catalytic mechanism of the *Dicistroviridae* RdRP have remain elusive. Here we reported crystal structures of two truncated forms of IAPV $3D^{pol}$, namely Δ85 and Δ40, both missing the NE region, and the $3D^{pol}$ protein in these structures exhibited three conformational states. The palm and thumb domains of these IAPV $3D^{pol}$ structures are largely consistent with those of the PV $3D^{pol}$ structures. However, in all structures, the RdRP fingers domain is partially disordered, while different conformations of RdRP substructures and interactions between them are also present. In particular, a large-scale conformational change occurred in the motif B-middle finger region in one protein chain of the Δ40 structure, while a previously documented alternative conformation of motif A was observed in all IAPV structures. These experimental data on one hand show intrinsic conformational variances of RdRP substructures, and on the other hand suggest possible contribution of the NE region in proper RdRP folding in IAPV.

1. Introduction

The *Dicistroviridae*, belonging to the *Picornavirales* order, is a virus family that contains many insect pathogens, and their host species include honeybees (Apis mellifera), true crickets (*Gryllidae*), triatomine bugs (*Reduviidae*), fire ants (*Solenopsis invicta*), and aphids (*Aphididae*). Honey bee diseases caused by dicistroviruses such as Israeli acute paralysis virus (IAPV) (Maori et al., 2007), Kashmir bee virus (KBV) (De Miranda et al., 2004), acute bee paralysis virus (ABPV) (Govan et al., 2000), deformed wing virus (Lanzi et al., 2006), and chronic bee paralysis virus (CBPV) (Bailey et al., 1963) can bring huge losses to apiculture. In particular, IAPV infection is considered an important trigger of honeybee colony collapse disorder (CCD) and can cause honeybee paralysis and death shortly after infection (Cox-Foster et al., 2007). Currently, there are no effective antiviral approaches for IAPV.

The positive-strand non-segmented RNA genome of dicistroviruses contains two open reading frames (ORFs), different from all other non-segmented *Picornavirales* species, such as the *Picornaviridae* poliovirus (PV), that only contain one ORF (Maori et al., 2007; De Miranda et al., 2010). Nevertheless, the two polyproteins and their proteolytically processed mature proteins encoded by dicistroviruses are highly homologous to picornavirus single polyprotein and corresponding mature proteins, respectively (Nakashima and Nakamura, 2008; Reddy et al., 2013) (Fig. 1A). Similar to the P2–P3 region of the PV polyprotein, IAPV ORF1 is responsible for production of mature proteins corresponding to PV 2A, 2B, 2C, 3A, 3B, 3C, and 3D. As documented in PV and other picornaviruses, these proteins likely participate in the viral replication complex (RC), in which the RNA-dependent RNA polymerase (RdRP) $3D^{pol}$ (pol denotes "polymerase") plays a central role in catalyzing the synthesis of genome-length RNA (Paul and Wimmer, 2015).

* Corresponding authors.
E-mail addresses: houchunsheng@caas.cn (C. Hou), gongpeng@wh.iov.cn (P. Gong).

https://doi.org/10.1016/j.virs.2023.05.002
Received 3 April 2023; Accepted 4 May 2023
Available online 6 May 2023

Since their discovery in the 1960s, viral RdRPs have become key systems for studying RNA viruses as well as developing anti-RNA virus strategies (Reich et al., 1961; Baltimore et al., 1963). In spite of a common right-hand polymerase core consisting palm, thumb, and fingers domains, the RdRP protein or protein complexes are quite diverse in size and composition, ranging from very compact 52 kDa PV 3D^{pol} to more than 400 kDa Crimean-Congo hemorrhagic fever virus (CCHFV) L protein that also harbors cap-snatching machinery and an ovarian tumor (OTU) protease module likely functioning in viral antagonism (Neufeld et al., 1991; Hansen et al., 1997; Thompson and Peersen, 2004; Frias-Staheli et al., 2007). On the other hand, all viral RdRPs share a structurally highly conserved polymerase active site typically including seven catalytic motifs A–G well documented in positive-strand RNA viruses (Gorbalenya et al., 2002; Bruenn, 2003). Among these motifs, highly conserved residues are found in palm motifs A, B, C, and fingers motif F with each of them contains one largely invariant residue (Gong, 2021). Motifs A and C each contains an aspartic acid residue invariant in all nucleic acid polymerases, responsible for two-divalent-metal-ion coordination critical for the nucleotidyl transfer reaction (Beese and Steitz, 1991). Motif B contains an invariant glycine that allows flipping of its amino peptide bond when the active site switches between catalytically open and closed states, while motif F includes an invariant arginine that contributes to both substrate ribonucleotide triphosphate (rNTP) binding and subsequent nucleotidyl transfer (Gong and Peersen, 2010; Shu and

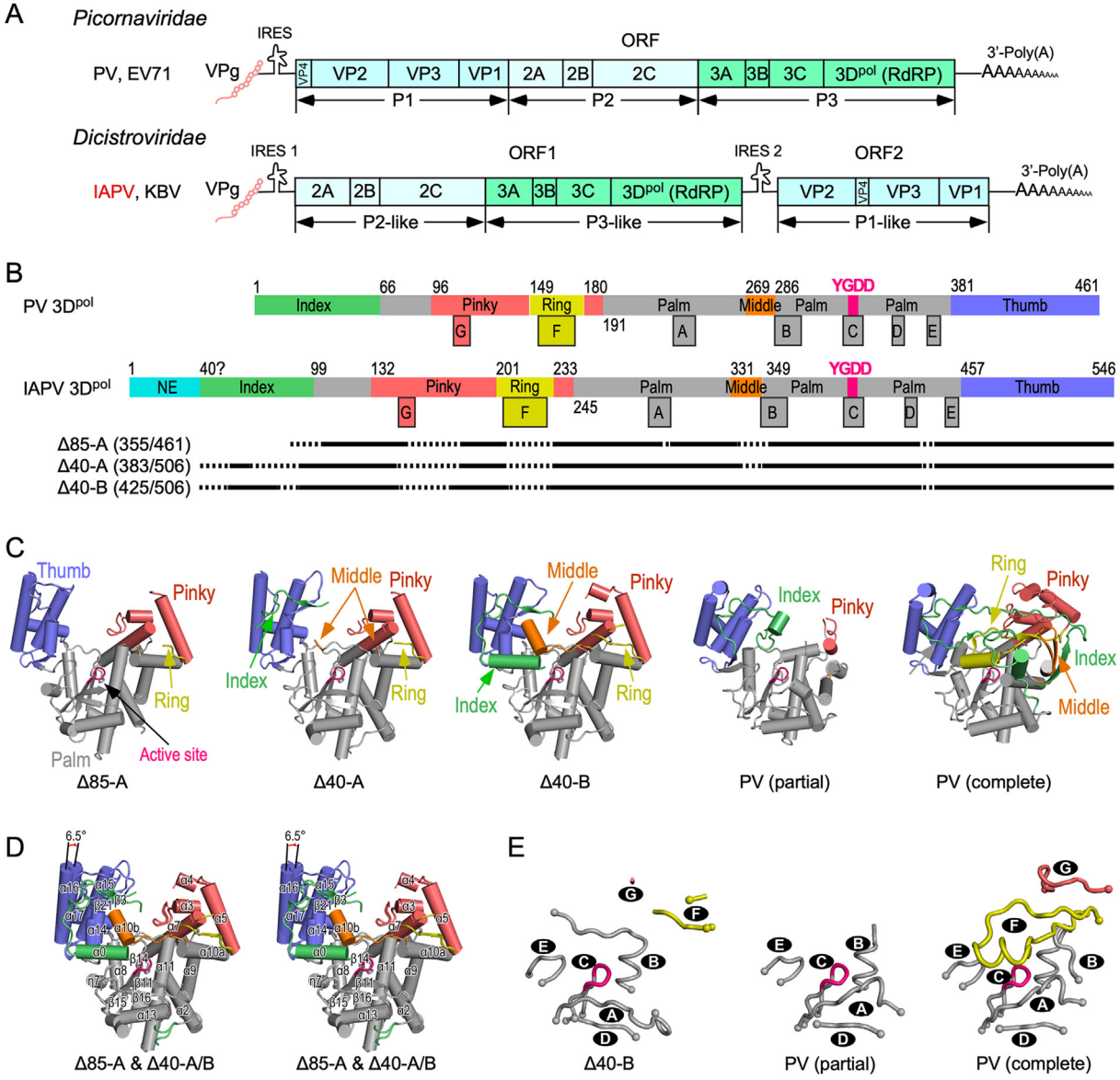

Fig. 1. Crystal structures of IAPV RdRPs Δ40 and Δ85 and comparisons with PV RdRP structures. **A** Comparison of the RNA genome organization of *Picornaviridae* and *Dicistroviridae*. VPg: viral protein genome-linked (corresponding to the 3B protein); IRES: internal ribosome entry site; ORF: open reading frame. Double arrows define P1–P2–P3 regions of the *Picornaviridae* polyprotein ORF and the corresponding regions in the *Dicistroviridae* genome. **B** Comparison of the 3D^{pol} proteins of PV and IAPV by defining structural and/or functional elements. Color coding: NE – cyan; index/middle/ring/pinky fingers – green/orange/yellow/pink; thumb – slate; palm – gray; YGDD signature sequence in the active site – magenta. RdRP motifs A–G are labeled by boxes with capital letters. Regions that are resolved or disordered in the IAPV 3D^{pol} structures are indicated by solid and dashed lines at the bottom of this panel. Numbers in parenthesis indicate resolved/total residues in each structure. Dashed lines indicate disordered regions. **C** Global view of IAPV Δ85-A, Δ40-A/B, and two forms of PV RdRP structures. The color coding is the same as in panel **B**. The structures are superimposed but shown separately. **D** Stereo-pair images of superposed three structures (Δ85, Δ40-A, and Δ40-B). Secondary structure assignment is based on the Δ40-B structure. **E** Comparison of catalytic motif conformations in representative IAPV and PV RdRP structures. The α-carbon atoms of terminal amino acids in each motif are shown as spheres. PDB entries: 1RDR (PV-partial), 1RA6 (PV-complete).

Gong, 2016; Li et al., 2022). Palm motifs D, E, and fingers motif G do not directly interact with NTP. Motif D is structurally associated with motif A and the backbones of these two motifs undergo coordinated movement, most prominent in positive-strand RNA viruses, also denoting the open and closed states of the active site (Gong and Peersen, 2010; Peersen, 2019). Motif E is located between the bottom of thumb and motifs C/A/D in the palm, and interacts with the product RNA backbone between positions −3 and −1, largely playing structural roles. As the only RdRP-unique motif, motif G interacts with the template RNA and plays an important role in restraining the template strand movement, presumably for precise positioning of the NTP for nucleotidyl transfer (Shu and Gong, 2016; Wang M. et al., 2020).

The 546-residue IAPV RdRP (herein termed 3D^{pol} according to picornavirus terminology) is moderately larger than the 461-residue PV 3D^{pol}. Sequence and structure homology analysis suggest that IAPV 3D^{pol} contains an N-terminal extension (NE) about 40-residue in length (Jia and Gong, 2019) (Fig. 1B). It has been documented that the very N-terminal glycine (G1) of PV 3D^{pol} plays a critical role in RdRP catalysis, presumably through participation of a structurally identified hydrogen-bonding network involving fingers domain residue G64 and motif A residues A239 and L241 and burying itself at the fingers–palm interface, while even adding 1–2 residues to the N-terminus of PV 3D^{pol} resulted in only trace amount of polymerase activity (Thompson and Peersen, 2004). Hence, the function of IAPV 3D^{pol} NE may be quite different, since it presumably cannot mimic the N-terminus of PV 3D^{pol}. In this work, we crystallized and determined the crystal structures of two forms of IAPV 3D^{pol}, namely Δ85 and Δ40, with deletion of N-terminal 85 and 40 residues, respectively. Three 3D^{pol} conformations were observed in these structures, all with the fingers domain only partially resolved. Structural analyses further revealed that several conserved RdRP substructures in the fingers and palm domains are quite dynamic, and some of them can even undergo previously unidentified large-scale movement and refolding. These structural findings on one hand advance our understandings of intra-molecular dynamics of viral RdRP in general, and on the other hand further suggest the critical role of the NE in IAPV 3D^{pol}'s structural integrity and function.

2. Materials and methods

2.1. Cloning and protein expression

The IAPV 3D^{pol} gene (isolate BJ2, GenBank entry: MG599488.1) was cloned into the pEASY-blunt-E1 vector containing an N-terminal hexahistidine tag. The N-terminal deletion mutants Δ40 and Δ85 of 3D^{pol} were constructed by a site-directed, ligase-independent mutagenesis (SLIM) method (Chiu et al., 2008). The full-length (FL) 3D^{pol}, Δ40, and Δ85 plasmids were transformed into *Escherichia coli* (*E. coli*) strain Trans B for the 3D^{pol} production. *E. coli* cells were grown at 37 °C overnight in LB medium with 100 μg/mL ampicillin (AMP100) and 50 μg/mL kanamycin (KAN50) until OD_{600} reached 1.0. The overnight culture was used to inoculate 1 L of LB medium with AMP100 and KAN50 to reach an initial OD_{600} of 0.025. The cells in LB medium were grown at 37 °C for approximately 3 h to reach an OD_{600} of 0.6–0.8 and then cooled to 25 °C before induction. Isopropyl-β-D-thiogalactopyranoside (IPTG) was added to a final concentration of 0.5 mmol/L, and the cells were grown for an additional 6 h before harvesting. After centrifuging at 6730 relative centrifugal force (RCF, or g-force) for 15 min at 4 °C, the harvested cells were resuspended in lysis buffer of 50 mmol/L Tris (pH 8.0), 300 mmol/L NaCl, 10 mmol/L imidazole, and 20% (vol/vol) glycerol and stored at −80 °C before purification.

2.2. Protein purification

The lysis buffer-resuspended cells were thawed and then lysed by passing through an AH-2010 homogenizer at 800–1000 bar (ATS Engineering Ltd.). NP40 (Sigma-Aldrich) was added to a final concentration of 0.1% (vol/vol) and then polyethylenimine (PEI) was added slowly over a 20-min period to a final concentration of 0.5% (vol/vol). The lysate was gently stirred at 4 °C for additional 15 min and then centrifuged for 1 h at 34400 RCF. The supernatant was filtered by 0.22 μm filters and loaded on a HisTrap HP column (GE Healthcare), and eluted by an elution buffer of 300 mmol/L NaCl, 50 mmol/L Tris (pH 8.0), 300 mmol/L imidazole, and 20% (vol/vol) glycerol. Fractions were pooled and diluted by a low-salt Q buffer of 25 mmol/L Tris (pH 8.5), 0.1 mmol/L EDTA, and 20% (vol/vol) glycerol to reach a final NaCl concentration of 60 mmol/L before loading on a HiTrap Q column (GE Healthcare) and eluting with a linear gradient from 60 mmol/L to 1 mol/L NaCl in 25 mmol/L Tris (pH 8.5), 0.1 mmol/L EDTA, and 20% (vol/vol) glycerol. Fractions were collected and concentrated to 1 mL and run over a Superdex 200 gel filtration column (GE Healthcare) equilibrated in a GF buffer of 600 mmol/L NaCl, 5 mmol/L Tris (pH 7.5), and 5% (vol/vol) glycerol. Pooled fractions were supplemented with tris-(2-carboxyethyl) phosphine (TCEP) to reach a final concentration of 5 mmol/L and concentrated before storage. Concentrated protein was flash frozen with liquid nitrogen as 5–10 μL aliquots and stored at −80 °C. The extinction coefficient was calculated based on protein sequence using the ExPASy ProtParam program (http://www.expasy.ch/tools/protparam.html) and used to determine the protein concentration. The typical yield is 5–10 mg of pure protein per liter of bacterial culture.

2.3. Protein crystallization, heavy-atom derivatization, data collection, and structure determination

Purified IAPV 3D^{pol} Δ85 and Δ40 were crystallized by the sitting-drop vapor diffusion method at 16 °C using 6–10 mg/mL protein samples. For Δ85 construct, hexagonal cylinder-shaped crystals grew after one day and reached final size in five days. Typically, 0.4 μL protein was mixed with 0.5 μL precipitant solution of 0.18–0.20 mol/L $MgCl_2$, 0.25 mmol/L $CdCl_2$, 0.08 mol/L Tris (pH 8.5–9.0), 14%–16% (wt./vol.) PEG4000, and 24–26% (vol/vol) glycerol. Some crystals were used for 10-min heavy-atom soaking with $(NH4)_2OsBr_6$ (Hampton Research) at 5 mmol/L concentration. For Δ40 construct, diamond-shape crystals appeared after two days and reached final size in a week. Typically, 0.4 μL protein was mixed with 0.4 μL precipitant solution of 1.70–1.72 mol/L $(NH_4)_2SO_4$ and 0.1 mol/L Bis-Tris (pH 5.0–5.5). Crystals for data collection were flash cooled in liquid nitrogen prior to data collection, and Δ40 crystals were transferred to a cryo-solution (precipitant solution supplemented with 25% (vol/vol) glycerol) by incremental buffer exchange prior to flash cooling. All data sets used for structure determination were collected at the Shanghai Synchrotron Radiation Facility (SSRF) beamline BL17U1 (wavelength: 0.9792 Å, temperature: 100 K). At least 180° of data for native crystals were typically collected in 0.5° oscillation steps and at least 360° of data were collected for heavy-atom soaked crystals. Reflections were integrated, merged, and scaled by HKL2000 (Otwinowski and Minor, 1997). Heavy-atom site identification and initial structure solution were done using SAD method and by AutoSol (Terwilliger et al., 2009). The initial model was generated by AutoBuild (Terwilliger et al., 2008). Multiple rounds of model rebuilding and structure refinement were done by Coot and PHENIX, respectively (Emsley and Cowtan, 2004; Liebschner et al., 2019). The 3500 K composite simulated-annealing omit $2F_o$-F_c electron density map were generated by program CNS (Brunger et al., 1998). Unless otherwise indicated, structure superpositioning were carried by THESEUS (Theobald and Wuttke, 2008). All RMSD calculations for structure similarity analyses were based on traditional least-square method.

2.4. Structural predictions by AlphaFold2

The structure of FL IAPV 3D^{pol} was predicted by AlphaFold2 (AF2, Jumper et al., 2021) with the following settings: template_mode = 0, msa_mode = mmseqs2_uniref_env, pair_mode = unpaired_paired, model_type = auto, num_recycles = auto, recycle_early_stop_tolerance = auto,

max_msa = auto, and num_seeds = 1. Five top models were generated with pLDDT (predicted local distance difference test) scores in a range of 91.9–92.4.

3. Results

3.1. IAPV 3D^{pol} structure determination and its structural overview

With an aim to solve the structure of IAPV 3D^{pol}, the FL 3D^{pol} and two N-terminal truncation mutants Δ40 and Δ85 were prepared, and the truncations were designed based on sequence homology with picornavirus 3D^{pol} and considerations of predicted secondary structures. Purified FL, Δ40, and Δ85 constructs were crystallized under different crystallization conditions, but only the two truncation constructs yielded atomic or near-atomic resolution X-ray diffractions. The Δ85 structure was solved in space group $P3_121$ at 2.70 Å resolution using osmium (Os) atom-based single-wavelength anomalous diffraction (SAD) method (Hendrickson, 2014) (Table 1). The Δ40 structure was solved in space group $P6_222$ at 3.25 Å resolution by molecular replacement (MR) method using the Δ85 structure as the search model (Tong and Rossmann, 1997) (Table 1).

In many viral RdRPs, the fingers domain can be further divided into index, middle, ring, and pinky subdomains according to the nomenclature first used in describing the complete structure of PV 3D^{pol} (Thompson and Peersen, 2004), and here we also use this nomenclature for better comparison with other RdRPs (Fig. 1B). With NE and part of index finger deleted, the Δ85 structure has relatively complete palm and thumb, but only has part of pinky finger and a short segment of ring finger resolved in the fingers domain (Fig. 1B and C). This structure is reminiscent of the first viral RdRP structure of PV that is also largely disordered in the fingers domain (Hansen et al., 1997) (Fig. 1C). For PV 3D^{pol}, the structural incompleteness is likely related to crystal packing involving inter-molecular interactions destabilizing fingers domain folding, since a mutant PV 3D^{pol} disrupting such interactions successfully yielded a complete structure in a subsequent study (Thompson and Peersen, 2004) (Fig. 1C). The Δ40 construct, containing all the PV-equivalent regions, crystallized in a different crystal form from that of Δ85 (i.e., differing in crystal packing) but still exhibited a partially disordered fingers domain (Fig. 1B–C). Unlike the Δ85 structure having a consistent conformation for both 3D^{pol} chains in the crystallographic asymmetric unit (chain A was chosen as the representative in Fig. 1), the two chains in the asymmetric unit of the Δ40 structure are quite different in the fingers domain. The chain A of the Δ40 structure (Δ40-A) is very similar to chain A of the Δ85 structure with a root-mean-square deviation (RMSD) of 0.74 Å (Δ85 structure as the reference and 95% residue coverage), except that a segment of the index finger tip was resolved and interacts with the top of thumb in a way similar to that observed in PV 3D^{pol} structures (Fig. 1B–C). By contrast, the middle finger is fully resolved in the chain B of the Δ40 structure (Δ40-B), albeit adopting a previously unidentified conformation (Fig. 1B–D, described in detail below). A typical hinging movement of thumb (about a 6.5° swing using helix α16 as the indicator) is observed between the Δ85 and Δ40 conformations, with thumb top in the latter moving inward (Fig. 1C and D). For the Δ85 structure missing the index-thumb interactions, a thumb loop (residues 479–486 connecting helices α14 and α15, α14–α15 loop) flips outward and partially occupies the position normally held by the index tip (Fig. 1C–D). Note that, neither of the IAPV 3D^{pol} structures has the fingers domain motifs F and G properly folded if using the canonical folding in the complete PV structure as the reference (Fig. 1E). In the following sections, we focus on the conformational dynamics and coordination of IAPV RdRP substructures in the context of known RdRP structures.

3.2. Crystal packing contributes to index tip conformation variation in IAPV 3D^{pol} structures

In the Δ40 structure, the completeness of the index tip is different in chains A and B. The resolved index finger segment (residues 56–67) in Δ40-A adopts a conformation consistent with that of the equivalent regions in Δ40-B and the complete PV 3D^{pol} structure (Fig. 2A–D). The resolved index segment in Δ40-B includes residues 55–82, with the C-terminal half adopting a helical conformation different from the

Table 1
X-ray diffraction data collection and structure refinement statistics.

Structure	Δ85-SAD	Δ85 PDB entry: 8IIB	Δ40 PDB entry: 8IIC
Data collection[a]			
Space group	$P3_121$	$P3_121$	$P6_222$
Cell dimensions			
a, *b*, *c* (Å)	150.5, 150.5, 104.6	150.5, 150.5, 104.6	167.9, 167.9, 218.3
α, β, γ (°)	90, 90, 120	90, 90, 120	90, 90, 120
Resolution (Å)[b]	25.0–3.15 (3.26–3.15)	23.8–2.70 (2.80–2.70)	23.8–3.25 (3.37–3.25)
No. of unique reflections	23,835	38,083	28,880
R_{merge}	0.10 (0.71)	0.041 (0.71)	0.071 (0.84)
R_{meas}	0.11 (0.73)	0.043 (0.75)	0.075 (0.88)
$CC_{1/2}$	1.000 (0.952)	0.995 (0.931)	0.993 (0.957)
$I/\sigma I$	28.8 (6.2)	57.9 (4.1)	31.1 (4.3)
Completeness (%)	100.0 (99.9)	100.0 (100.0)	98.8 (98.5)
Redundancy	18.8 (21.1)	10.1 (10.6)	10.2 (10.5)
Structure refinement			
Resolution (Å)		2.70	3.25
No. of unique reflections		37,085	27,744
R_{work}/R_{free}[c] (%)		21.3/25.4	21.1/24.6
No. atoms			
Protein		2705	3055
Ligand/ion/water		–/19/193	–/–/7
***B*-factor (Å^2)**			
Protein		40.7	51.8
Ligand/ion/water		/50.9/36.3	–/–/32.4
R.m.s. deviations			
Bond lengths (Å)		0.008	0.011
Bond angles (°)		1.094	1.228
Ramachandran stat.[d]		90.0/9.5/0.2/0.3	88.3/10.8/0.4/0.5

[a] One crystal was used for data collection.
[b] Values in parentheses are for highest-resolution shell.
[c] 5% of data are taken for the R_{free} set.
[d] Values are in percentage and are for most favored, additionally allowed, generously allowed, and disallowed regions in Ramachandran plots, respectively.

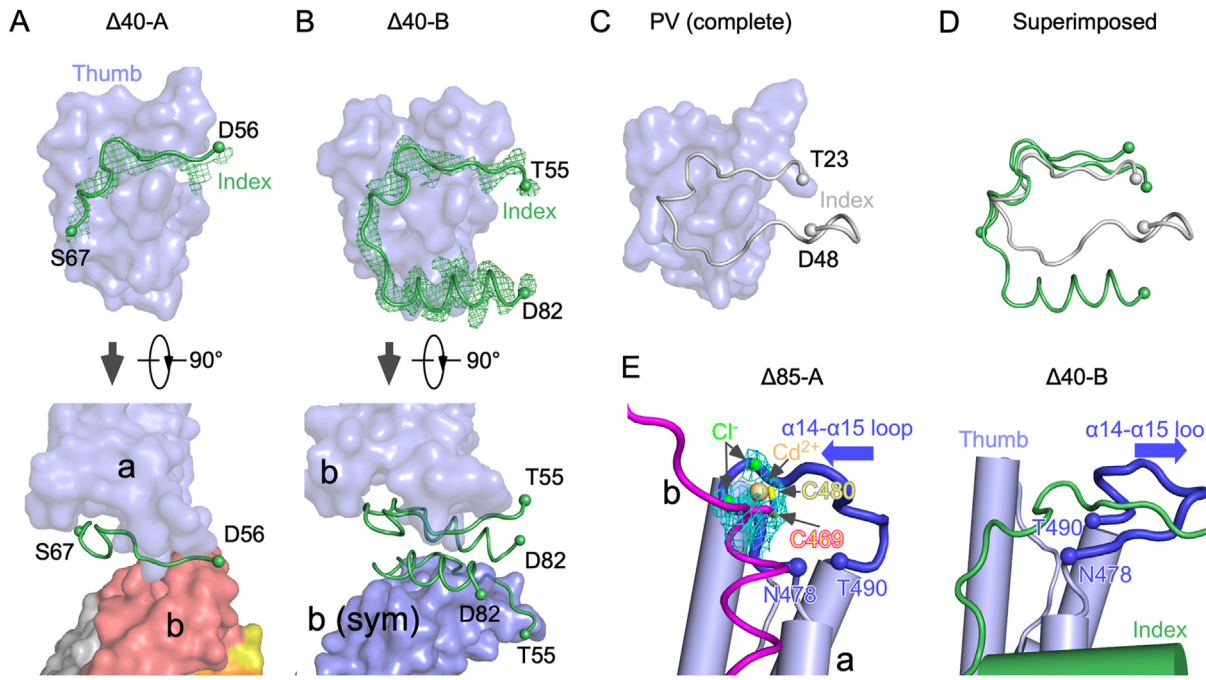

Fig. 2. Variation of IAPV RdRP index tip conformation and possible contribution of crystal packing. **A**–**D** Comparison of RdRP index finger tip conformation of IAPV Δ40-A (**A**), Δ40-B (**B**), and PV (**C**, PDB entry: 1RA6). The structures are superimposed (**D**) and shown separately in panels **A**–**C**. The α-carbon atoms of terminal amino acids of the shown index finger tip are shown in spheres. Top: **A**–**C**, only thumb (surface) and index tip (cartoon) are shown; **D**: only index tip is shown. Bottom: protein-protein interactions involving the index tip in the IAPV Δ40 crystal lattice. Lower case letters indicate chain assignment. "sym": a crystallographic symmetry-related molecule. The 3500 K composite SA-omit electron density maps (contoured at 1.2 σ) for the resolved index finger region are overlaid on the structural models in panels A–B. **E** Comparison of crystal packing near the top of thumb in Δ85-A (left) and Δ40-B (right). The α14–α15 thumb loop (in blue) in Δ85-A adopts an alternative conformation, likely due to a Cd^{2+}-mediated crystal packing between chain a and chain b (in magenta). The 3500 K composite SA-omit electron density map (contoured at 1.5 σ) for the Cd^{2+} and its coordination partners is overlaid on the structural model. The Cd^{2+} and Cl^{-} are shown as spheres. In the Δ40-B structure, the α14–α15 loop adopts the regular conformation, allowing interactions with the index tip. The α-carbon atoms of terminal amino acids of the α14–α15 loop are shown as spheres.

corresponding region in the PV $3D^{pol}$ structure (Fig. 2B–D). The incompleteness and conformational variation observed in the IAPV Δ40 structure are likely related crystal packing interactions. In Δ40-A, the PV-like trajectory of the index finger beyond residue 67 is blocked by the neighboring Δ40-B pinky finger (Fig. 2A), while the non-canonical helical substructure in Δ40-B index interacts with the same region of a symmetry-related Δ40-B (Fig. 2B). In the majority of viral RdRPs, the tip of index finger interacts with the top of thumb, encircling the right-hand structure (Lesburg et al., 1999; Thompson and Peersen, 2004; Gong, 2021). Nevertheless, this viral RdRP signature thumb-index tip interactions are retained in both chains of the Δ40 structure. By contrast, the missing of such interactions in the Δ85 structure is likely a result of the crystal packing interactions between thumb residues 469–480 of chains A and B. Two clusters of cadmium ion (Cd^{2+})-mediated tetrahedral coordination likely play a key role in maintaining these pseudo-2-fold related inter-molecular interactions (Fig. 2E). The α14–α15 loop is partly involved in the coordination interactions and therefore adopts a conformation different from that typically observed in RdRP structures with thumb-index tip interactions (Fig. 2E). Note that, Cd^{2+} is required for Δ85 crystal growth (see Materials and Methods), further suggesting the relationship between crystal packing and the disorder of the entire Δ85 index finger tip.

3.3. An alternative conformation of motif A observed in IAPV RdRP structures

RdRP motif A is an extended substructure, with its N-terminal half participating in divalent metal ion binding during the nucleotidyl transfer reaction, and the C-terminal half containing a highly conserved aspartic acid residue (D294 in IAPV $3D^{pol}$, four residues away from the invariant D289) that plays a critical role in NTP 2′-hydroxyl recognition and RdRP active site closure (Gong and Peersen, 2010; Shu and Gong, 2016). The canonical fold of motif A is observed in the majority of RdRP structures, with the backbone around the C-terminal aspartic acid residue bending toward the active site (Fig. 3A). Opening and closing of the active site are accompanied by the backbone shift of the N-terminal half of motif A, as suggested by RdRP catalytic complexes in PV, EV71, and HCV (Gong and Peersen, 2010; Appleby et al., 2015; Shu and Gong, 2017; Peersen, 2019; Li et al., 2022), but this conformational change does not alter the basic folding and the interactions between motif A, the neighboring motif B loop (residues 346–353) and middle finger (Fig. 3B). By contrast, motif A in the IAPV $3D^{pol}$ structures adopts an alternative conformation with its C-terminal half flipped away from the active site (Fig. 3B). As a result, the C-terminal aspartic acid residue (D294) is either disordered (Δ85) or pointing outward (Δ40). This alternative conformation of motif A has been only observed in the encephalomyocarditis virus (EMCV) $3D^{pol}$ crystal structure, while another crystal form of the same protein exhibits regular motif A conformation (Vives-Adrian et al., 2014) (Fig. 3, A–B, EMCV structures). For both EMCV and IAPV structures, the contribution of crystal packing interactions to this alternative conformation is not evident.

The observation of the alternative motif A conformations in two evolutionarily-distant *Picornavirales* RdRPs (*Picornaviridae* EMCV and *Dicistroviridae* IAPV) further suggests common and intrinsic dynamics of motif A (Bi et al., 2017). Very interestingly, the motif B loop and middle finger exhibit two dramatically different conformations when motif A adopts the alternative conformation. In the IAPV Δ85 structure, canonical folding of motif B loop is retained and middle finger is disordered. By contrast, in the IAPV Δ40 structure, the corresponding region adopts a very different conformation (described in detail in the next section), further suggesting the coordination between motifs A/D and motif B/middle finger in RdRP folding.

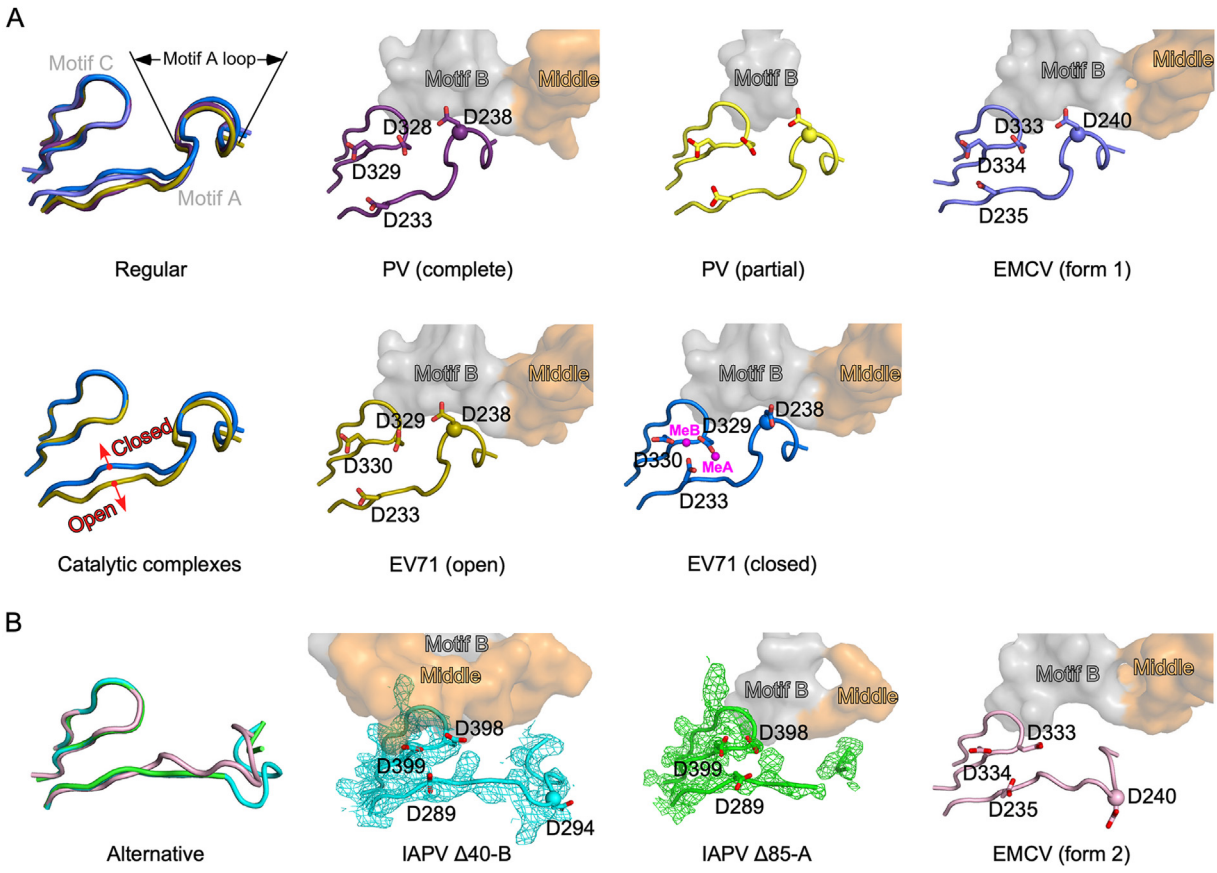

Fig. 3. An alternative conformation of motif A observed in IAPV RdRP Δ40 and Δ85 structures. **A** Regular conformations of motif A observed in PV, EV71, and EMCV RdRPs. Structure superimpositions (top left) indicate a consistent conformation of motif A loop. The "open" and "closed" states are assigned for RdRP catalytic complexes (second row) according to the mechanisms of RdRP nucleotide addition cycle. **B** The alternative conformation of motif A observed in IAPV and EMCV RdRP structures. In separately shown structures, motif B and middle finger are shown as spheres to highlight its crosstalk with motif A (also see Fig. 4), and the side chains of key aspartic acid residues in motifs A and C are shown as sticks. The α-carbon atom of the motif A loop aspartic acid residue is shown as spheres. The 3500 K composite SA-omit electron density maps (contoured at 1.5 σ) for the motifs A and C are overlaid on IAPV structural models. The Δ85-A structure is manually oriented. PDB entries: 1RA6 (PV-complete), 1RDR (PV-partial), 4NZ0 (EMCV-form 1), 5F8G (EV71-open), 5F8J (EV71-closed), 4NYZ (EMCV-form 2).

3.4. Refolding of motif B loop and middle finger allows establishment of interactions with the thumb and index finger

Viral RdRP motif B comprises an N-terminal loop and a C-terminal helix, with the N-terminal two residues (G285-M286 in PV) forming antiparallel β-type interactions with two residues (D238-A239 in PV) in the C-terminal half of motif A in the canonical RdRP fold (Fig. 4A). These interactions between motif B and motif A are critical for RdRP catalytic activities, as the motif B loop contains the highly conserved Ser-Gly (residues 288–289 in PV), and the C-terminal aspartic acid of motif A directly participates in NTP recognition. The middle finger is usually a β-hairpin structure co-folding with the index and ring fingers to form an anti-parallel 5-stranded β-sheet (Lesburg et al., 1999; Thompson and Peersen, 2004). The C-terminal end of middle finger connects to the

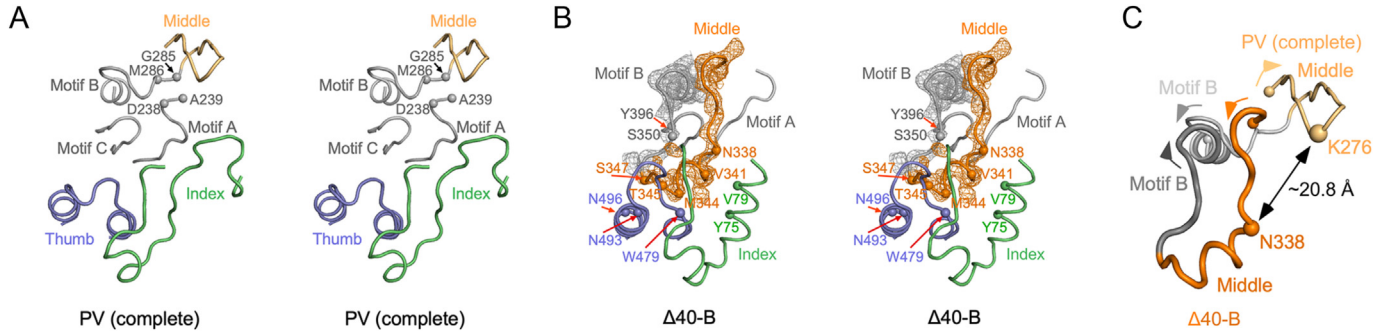

Fig. 4. A previously unidentified conformation of the middle finger observed in IAPV Δ40-B RdRP structure. **A**–**B** Stereo-pair images of the complete PV structure (**A**) and IAPV Δ40-B (**B**) structure with 3500 K composite SA-omit electron density map (contoured at 1.2 σ) overlaid on the middle finger and motif B of the latter. For clarity, only motifs A/B/C, middle finger, and part of the index finger and thumb are shown. The α-carbon atoms of key residues involved in interactions between RdRP components are shown as spheres. **C** Superimposition of only the middle finger and motif B of the two structures highlighting the large scale conformational change. Arrows indicate peptide trajectories. The α-carbon atoms of two equivalent residues (PV K276 and IAPV N338) are shown as large spheres to highlight the scale of the conformational difference. PDB entry: 1RA6 (PV-complete).

N-terminus of the motif B loop. In the Δ85 structure, the motif B loop is largely disordered, while in the Δ40 structure, the motif B loop swings about 90° from the canonical position toward the thumb and establishes new interactions with motif C involving residues S350 (within the motif B SG signature sequence) and Y296 (within the motif C YGDD signature sequence) (Fig. 4B). Very interestingly, the entire middle finger refolds with the motif B loop and establishes a mixture of hydrophobic and polar interactions with both thumb and index finger in the Δ40-B structure (Fig. 4B). In such a structure, the middle finger no longer adopts β-type structure and refolds as a combination of an N-terminal loop and a C-terminal helix. More specifically, middle finger residues S340/V341 and M344/T345/S347 interact with index finger residues Y75/V79 and thumb residues W479/N493/N496, respectively (Fig. 4B). Using the complete PV 3D^{pol} structure as the reference, some middle finger residues move over a distance longer than 20 Å between the two conformational states (Fig. 4C, primary structure equivalent PV residue K276 and IAPV residue N338 are used as an example). This large conformational change of the RdRP middle finger has not been observed in any other viral RdRP systems. Although the RdRP conformation in Δ40-B is probably catalytically incompetent due to the misplacement of several key catalytic residues, it nevertheless highlights the large scale and capacity of substructure dynamics and coordination among the palm–fingers–thumb framework of viral RdRPs.

3.5. *Two spatially related inter-motif regions exhibit diversity in sequence and structure*

The inter-motif region between RdRP motifs B and C (termed region B–C) has been documented to exhibit high-level sequence and structural diversity (Yang et al., 2021). We therefore compared region B–C and the

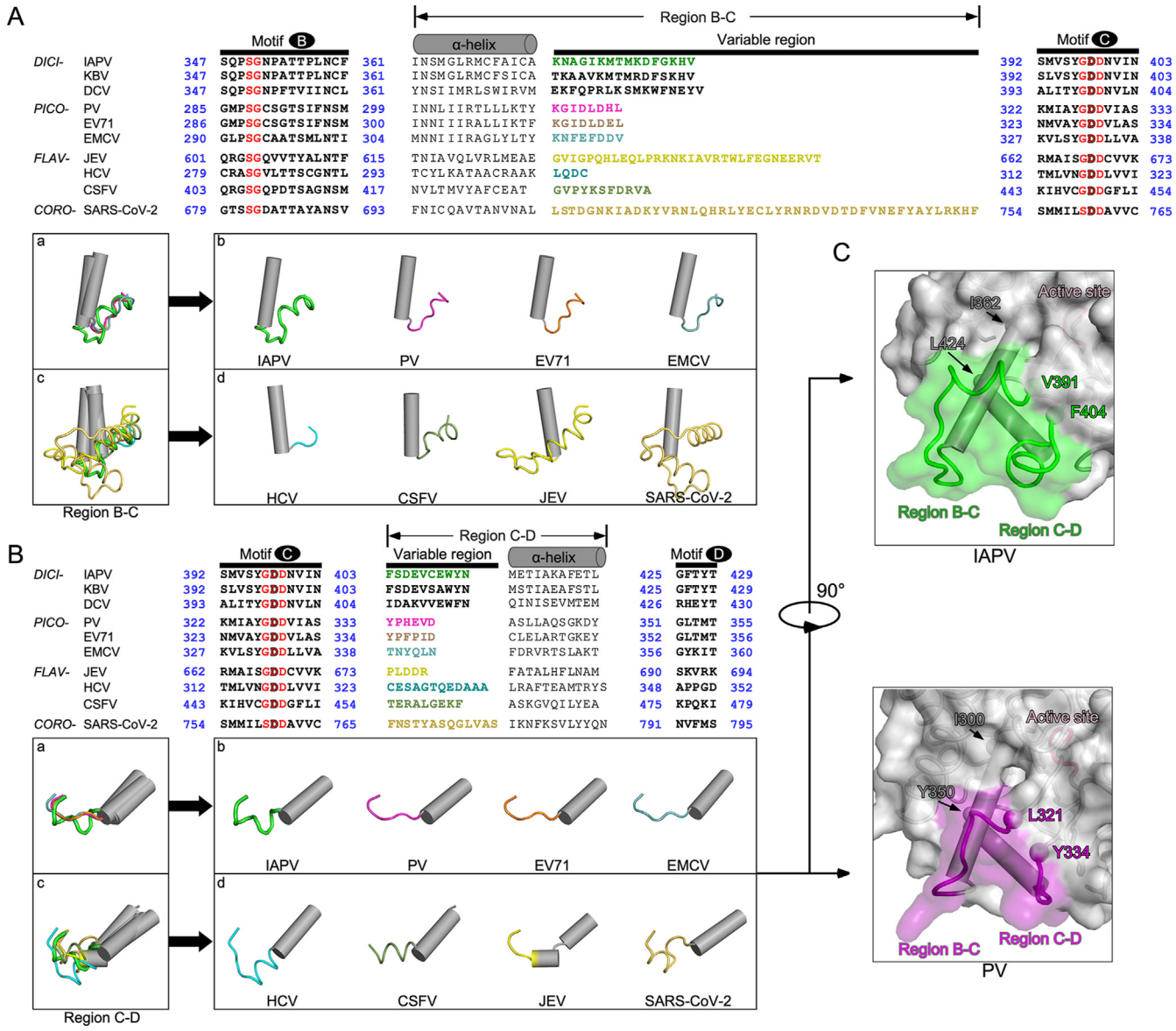

Fig. 5. Diversity in sequence and structure of two inter-motif regions in representative RdRPs in positive-strand RNA viruses. **A**–**B** Top: sequence alignment of RdRP motifs B/C (panel **A**) and C/D (panel **B**) with the corresponding inter-motif regions. Bottom: a structural comparison of inter-motif regions of representative RdRPs in *Picornavirales* (first row) and positive-strand RNA viruses (second row). Structures are shown in superimposed manner (left) and individually (right). DICI: *Dicistroviridae*, PICO: *Picornaviridae*; FLAV: *Flaviviridae*; CORO: *Coronaviridae*. The signature sequences in motifs B and C are shown in red and the RdRP-invariant aspartic acid residue in motif C is further highlighted by black edge. The loop radius of IAPV structure is thicker than those of other viruses. **C** A structural comparison of the bottom of RdRP palm in IAPV and PV, with the two inter-motif regions in green and magenta, respectively. The α-carbon atoms of terminal residues of each inter-motif regions are shown as spheres. The views of panels B and C are correlated by a rotation of 90°. A combination of surface and cartoon representations are used. PDB entries: 1RA6 (PV), 5F8G (EV71), 4NZ0 (EMCV), 1NB7 (HCV), 5YF5 (CSFV), 4K6M (JEV), 7C2K (SARS-CoV-2).

spatially neighboring region C–D (i.e., the region between motifs C and D) of IAPV 3D^{pol} structures with the corresponding RdRP regions in representative positive-strand RNA viruses (Fig. 5). The *Distroviridae* region B–C is about 8–9 residues longer than that of *Picornaviridae*, but much shorter than those of *Flavivirus* and *Coronaviridae* (Fig. 5A). Similarly, the IAPV 3D^{pol} region B–C structure (consistent in Δ85 and Δ40) adopts a helix-turn-helix structure with a complexity between the more compact PV structure and the more complicated Japanese encephalitis virus (JEV) and severe acute respiratory syndrome coronavirus 2 (SARS-CoV-2) structures (Thompson and Peersen, 2004; Lu and Gong, 2013; Gao et al., 2020) (Fig. 5A). The overall sequence-length variation of region C–D is not as high as that of region B–C, and does not follow the trend observed in region B–C (Fig. 5A–B). The *Dicistroviridae* region C–D is 4–5 residues longer than its *Picornaviridae* and *Flavivirus* counterparts, comparable to that of *Pestivirus* classical swine fever virus (CSFV), and 3–4 residues shorter than that of HCV and SARS-CoV-2 (Lesburg et al., 1999; Liu et al., 2018; Gao et al., 2020) (Fig. 5B). Structurally, the IAPV region C–D can also be clearly distinguished from those of other viral families (Fig. 5B). Since regions B–C and C–D co-fold at the bottom of the palm domain, they could possibly together mediate versatile protein-protein interactions due to their structural and sequence diversity among RNA viruses (Fig. 5C).

4. Discussion

No matter how diverse the RdRP overall architecture is, proper protein folding to allow viral RdRP catalytic motifs to adopt canonical conformations around the active site is critical for catalytic activities. While in PV proper folding is achieved as shown in the complete 3D^{pol} crystal structure (Thompson and Peersen, 2004), IAPV RdRP structures reported here suggest that either its NE or other viral proteins may play essential roles to achieve such proper folding (Fig. 6A–B). Flavivirus RdRP protein NS5 contains a methyltransferase that is connected to the RdRP core by a 10-residue linker and a ~30-residue NE (same term but no sequence homology to IAPV NE). Removal of the MTase part of NS5 impairs RdRP initiation activities, while further removal of the linker and NE results in the loss of regular polymerase activities (Wu et al., 2015, 2023). Structurally, the flavivirus NE co-folds with the index, pinky, and palm, while in two types of full-length NS5 global conformations, the MTase can interact with the index, middle, and ring (Egloff et al., 2007; Lu and Gong, 2013; Zhao et al., 2015) (Fig. 6, C–D). Coronavirus RdRP protein nsp12 contains an N-terminal NiRAN (originally named for nidovirus RdRP-associated nucleotydyltransferase) domain that is involved in viral RNA capping, and an "interface" region that connects the RdRP core and NiRAN (Lehmann et al., 2015; Gao et al., 2020; Walker et al., 2021). These two regions mainly interact with RdRP palm and fingers, respectively, likely contributing to the folding of the RdRP core. However, a functioning RdRP can be assembled only with one nsp7 and two nsp8 proteins co-folding with nsp12 (Gao et al., 2020; Hillen et al., 2020; Wang Q. et al., 2020). The non-canonical RdRP folding observed in the IAPV 3D^{pol} structures indicates that the NE could play critical roles for RdRP structure and function either alone or with the help of other proteins involved in the viral RC.

Deep learning-based protein structure prediction has brought revolutionary impact to biological science. In order to better understand our experimental data, we performed structure prediction of the full-length IAPV 3D^{pol} using AlphaFold2 (AF2) (Jumper et al., 2021). The top five AF2 models are largely consistent, with the most variable region indeed being the NE (Fig. 6E). In these models, the N-terminus (residues 1–7) interacts with the ring finger root, and the C-terminus (residues 30–38) interacts with the index and middle fingers. The rest of NE (residues 8–29) does not have established interactions with the RdRP core in these models and is the most variable part. The structural features of NE in the AF2-predicted models also support the requirement of other component(s) of the RC to fulfill RdRP function. Although the NE exhibits uncertainties, the AF2-derived RdRP core is convergent and adopts the canonical fold. If using the complete PV 3D^{pol} structure as the reference model, the AF2-derived IAPV RdRP core has an RMSD of 2.1 Å (90% residue coverage) (Fig. 6F). The alternative conformations of motif A, motif B, middle finger, and index finger observed in IAPV Δ40 and Δ85 crystal structures are not present in the AF2-derived models.

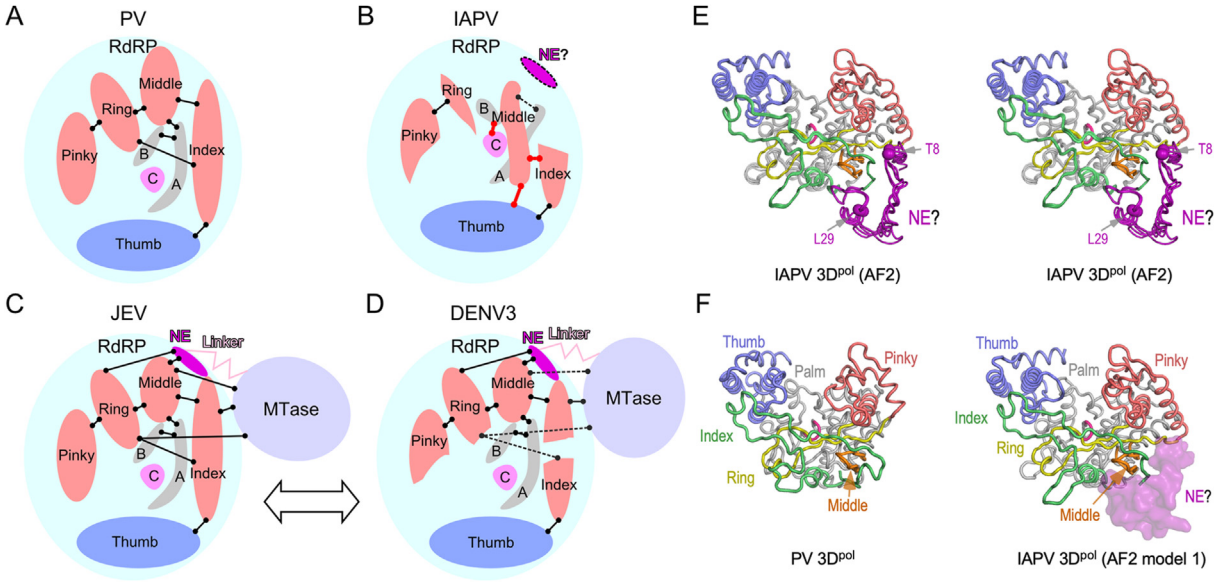

Fig. 6. The NE region likely contributes to proper folding and polymerase function of IAPV RdRP. **A**–**D** Cartoon illustration of RdRP components and crosstalk among them (solid lines) in PV (**A**), IAPV (**B**), JEV (**C**) and dengue virus 3 (DENV3) (**D**). With the NE region deleted, parts of the IAPV RdRP fingers domain are disordered and some interactions are lost (dashed lines), while motifs A/B, index and middle can adopt alternative conformations and establish new interactions (thick red lines). For flaviviruses, there are two modes of global conformation of the RdRP protein NS5 represented by JEV and DENV3 structures. **E** Superimposition of AF2-predicted top models indicate structural diversity of NE in stereo-pair mode. The most variable part of NE is indicated by the terminal residues (α-carbon atoms in spheres). **F** Except for the structural uncertainty of NE region (in surface representation), the folding of AF2-derived IAPV model(s) are highly consistent with that of the complete PV crystal structure. The color coding for RdRP components is the same as in Fig. 1. PDB entry: 1RA6 (PV).

5. Conclusions

In summary, the experimentally obtained incomplete IAPV 3D^{pol} structures in this work enriches the general understandings of conformational dynamics of RdRP core components and implies critical roles of the NE in a context of viral RC for a fully functional RdRP. The structural data presented here provides an important reference for further enzymology and virology studies in IAPV. Attempts to solve a structure of a complete dicistrovirus RdRP or its catalytic complex are needed to clarify such roles of NE and for better comparison with the picornavirus RdRPs.

Data availability

Atomic coordinates and structure factors for the reported crystal structures have been deposited in the Protein Data Bank under accession codes 8IIB (Δ85) and 8IIC (Δ40).

Ethics statement

This article does not contain any studies involved human or animal subjects.

Author contributions

Xiang Fang: investigation, data curation, formal analysis, visualization, writing-original draft, writing-review and editing. Guoliang Lu: formal analysis, investigation, writing-review and editing. Yanchun Deng: investigation, writing-review and editing. Sa Yang: investigation, writing-review and editing. Chunsheng Hou: conceptualization, funding acquisition, resources, supervision, writing-review and editing. Peng Gong: conceptualization, data curation, formal analysis, supervision, writing-original draft, writing-review and editing, funding acquisition. All the authors read and approved the manuscript.

Conflict of interest

Prof. Peng Gong is an editorial board member for Virologica Sinica and was not involved in the editorial review or the decision to publish this article. The authors declare no competing interests.

Acknowledgments

We thank Dr. Li Zhang, Shuai Deng, Qiaojie Liu, and Shunli Liu for laboratory assistance, synchrotron SSRF (beamlines BL17U1, BL19U1, and BL10U2, Shanghai, China) for access to beamlines, and the Institutional Center for Shared Technologies and Facilities, Wuhan Institute of Virology, Chinese Academy of Sciences for access to instruments. This work was supported by the National Natural Science Foundation of China (31802147 to G.L.; 31572471, 31811530276 to C.H.), National Key Research and Development Program of China (2018YFA0507200 to P.G. and G.L.), the Agricultural Science and Technology Innovation Program (CAAS-ASTIP-2023-IBFC to C.H.), the Creative Research Group Program of Natural Science Foundation of Hubei Province (2022CFA021 to P.G.), the Central Public-Interest Scientific Institution Basal Research Fund (Y2021YJ25 to C.H.) and Key Biosafety Science and Technology Program of Hubei Jiangxia Laboratory (JXBS001 to P.G.).

References

Appleby, T.C., Perry, J.K., Murakami, E., Barauskas, O., Feng, J., Cho, A., Fox 3rd, D., Wetmore, D.R., Mcgrath, M.E., Ray, A.S., Sofia, M.J., Swaminathan, S., Edwards, T.E., 2015. Viral replication. Structural basis for RNA replication by the hepatitis C virus polymerase. Science 347, 771–775.

Bailey, L., Gibbs, A.J., Woods, R.D., 1963. Two viruses from adult honey bees (*Apis mellifera* Linnaeus). Virology 21, 390–395.

Baltimore, D., Eggers, H.J., Franklin, R.M., Tamm, I., 1963. Poliovirus-induced RNA polymerase and the effects of virus-specific inhibitors on its production. Proc. Natl. Acad. Sci. U. S. A. 49, 843–849.

Beese, L.S., Steitz, T.A., 1991. Structural basis for the 3′-5′ exonuclease activity of *Escherichia coli* DNA polymerase I: a two metal ion mechanism. EMBO J. 10, 25–33.

Bi, P., Shu, B., Gong, P., 2017. Crystal structure of the coxsackievirus A16 RNA-dependent RNA polymerase elongation complex reveals novel features in motif A dynamics. Virol. Sin. 32, 548–552.

Bruenn, J.A., 2003. A structural and primary sequence comparison of the viral RNA-dependent RNA polymerases. Nucleic Acids Res. 31, 1821–1829.

Brunger, A.T., Adams, P.D., Clore, G.M., Delano, W.L., Gros, P., Grosse-Kunstleve, R.W., Jiang, J.S., Kuszewski, J., Nilges, M., Pannu, N.S., Read, R.J., Rice, L.M., Simonson, T., Warren, G.L., 1998. Crystallography & NMR system: a new software suite for macromolecular structure determination. Acta Crystallogr. D Biol. Crystallogr. 54, 905–921.

Chiu, J., Tillett, D., Dawes, I.W., March, P.E., 2008. Site-directed, Ligase-Independent Mutagenesis (SLIM) for highly efficient mutagenesis of plasmids greater than 8kb. J. Microbiol. Methods 73, 195–198.

Cox-Foster, D.L., Conlan, S., Holmes, E.C., Palacios, G., Evans, J.D., Moran, N.A., Quan, P.L., Briese, T., Hornig, M., Geiser, D.M., Martinson, V., Vanengelsdorp, D., Kalkstein, A.L., Drysdale, A., Hui, J., Zhai, J., Cui, L., Hutchison, S.K., Simons, J.F., Egholm, M., Pettis, J.S., Lipkin, W.I., 2007. A metagenomic survey of microbes in honey bee colony collapse disorder. Science 318, 283–287.

De Miranda, J.R., Cordoni, G., Budge, G., 2010. The Acute bee paralysis virus-Kashmir bee virus-Israeli acute paralysis virus complex. J. Invertebr. Pathol. 103 (Suppl. 1), S30–S47.

De Miranda, J.R., Drebot, M., Tyler, S., Shen, M., Cameron, C.E., Stoltz, D.B., Camazine, S.M., 2004. Complete nucleotide sequence of Kashmir bee virus and comparison with acute bee paralysis virus. J. Gen. Virol. 85, 2263–2270.

Egloff, M.P., Decroly, E., Malet, H., Selisko, B., Benarroch, D., Ferron, F., Canard, B., 2007. Structural and functional analysis of methylation and 5′-RNA sequence requirements of short capped RNAs by the methyltransferase domain of dengue virus NS5. J. Mol. Biol. 372, 723–736.

Emsley, P., Cowtan, K., 2004. Coot: model-building tools for molecular graphics. Acta Crystallogr. D Biol. Crystallogr. 60, 2126–2132.

Frias-Staheli, N., Giannakopoulos, N.V., Kikkert, M., Taylor, S.L., Bridgen, A., Paragas, J., Richt, J.A., Rowland, R.R., Schmaljohn, C.S., Lenschow, D.J., Snijder, E.J., Garcia-Sastre, A., Virgin, H.W.T., 2007. Ovarian tumor domain-containing viral proteases evade ubiquitin- and ISG15-dependent innate immune responses. Cell Host Microbe 2, 404–416.

Gao, Y., Yan, L., Huang, Y., Liu, F., Zhao, Y., Cao, L., Wang, T., Sun, Q., Ming, Z., Zhang, L., Ge, J., Zheng, L., Zhang, Y., Wang, H., Zhu, Y., Zhu, C., Hu, T., Hua, T., Zhang, B., Yang, X., Li, J., Yang, H., Liu, Z., Xu, W., Guddat, L.W., Wang, Q., Lou, Z., Rao, Z., 2020. Structure of the RNA-dependent RNA polymerase from COVID-19 virus. Science 368, 779–782.

Gong, P., 2021. Structural basis of viral RNA-dependent RNA polymerase nucleotide addition cycle in picornaviruses. Enzymes 49, 215–233.

Gong, P., Peersen, O.B., 2010. Structural basis for active site closure by the poliovirus RNA-dependent RNA polymerase. Proc. Natl. Acad. Sci. U. S. A. 107, 22505–22510.

Gorbalenya, A.E., Pringle, F.M., Zeddam, J.L., Luke, B.T., Cameron, C.E., Kalmakoff, J., Hanzlik, T.N., Gordon, K.H., Ward, V.K., 2002. The palm subdomain-based active site is internally permuted in viral RNA-dependent RNA polymerases of an ancient lineage. J. Mol. Biol. 324, 47–62.

Govan, V.A., Leat, N., Allsopp, M., Davison, S., 2000. Analysis of the complete genome sequence of acute bee paralysis virus shows that it belongs to the novel group of insect-infecting RNA viruses. Virology 277, 457–463.

Hansen, J.L., Long, A.M., Schultz, S.C., 1997. Structure of the RNA-dependent RNA polymerase of poliovirus. Structure 5, 1109–1122.

Hendrickson, W.A., 2014. Anomalous diffraction in crystallographic phase evaluation. Q. Rev. Biophys. 47, 49–93.

Hillen, H.S., Kokic, G., Farnung, L., Dienemann, C., Tegunov, D., Cramer, P., 2020. Structure of replicating SARS-CoV-2 polymerase. Nature 584, 154–156.

Jia, H., Gong, P., 2019. A structure-function diversity survey of the RNA-dependent RNA polymerases from the positive-strand RNA viruses. Front. Microbiol. 10, 1945.

Jumper, J., Evans, R., Pritzel, A., Green, T., Figurnov, M., Ronneberger, O., Tunyasuvunakool, K., Bates, R., Zidek, A., Potapenko, A., Bridgland, A., Meyer, C., Kohl, S.a.A., Ballard, A.J., Cowie, A., Romera-Paredes, B., Nikolov, S., Jain, R., Adler, J., Back, T., Petersen, S., Reiman, D., Clancy, E., Zielinski, M., Steinegger, M., Pacholska, M., Berghammer, T., Bodenstein, S., Silver, D., Vinyals, O., Senior, A.W., Kavukcuoglu, K., Kohli, P., Hassabis, D., 2021. Highly accurate protein structure prediction with AlphaFold. Nature 596, 583–589.

Lanzi, G., De Miranda, J.R., Boniotti, M.B., Cameron, C.E., Lavazza, A., Capucci, L., Camazine, S.M., Rossi, C., 2006. Molecular and biological characterization of deformed wing virus of honeybees (*Apis mellifera* L.). J. Virol. 80, 4998–5009.

Lehmann, K.C., Gulyaeva, A., Zevenhoven-Dobbe, J.C., Janssen, G.M., Ruben, M., Overkleeft, H.S., Van Veelen, P.A., Samborskiy, D.V., Kravchenko, A.A., Leontovich, A.M., Sidorov, I.A., Snijder, E.J., Posthuma, C.C., Gorbalenya, A.E., 2015. Discovery of an essential nucleotidylating activity associated with a newly delineated conserved domain in the RNA polymerase-containing protein of all nidoviruses. Nucleic Acids Res. 43, 8416–8434.

Lesburg, C.A., Cable, M.B., Ferrari, E., Hong, Z., Mannarino, A.F., Weber, P.C., 1999. Crystal structure of the RNA-dependent RNA polymerase from hepatitis C virus reveals a fully encircled active site. Nat. Struct. Biol. 6, 937–943.

Li, R., Wang, M., Gong, P., 2022. Crystal structure of a pre-chemistry viral RNA-dependent RNA polymerase suggests participation of two basic residues in catalysis. Nucleic Acids Res. 50, 12389–12399.

Liebschner, D., Afonine, P.V., Baker, M.L., Bunkoczi, G., Chen, V.B., Croll, T.I., Hintze, B., Hung, L.W., Jain, S., Mccoy, A.J., Moriarty, N.W., Oeffner, R.D., Poon, B.K., Prisant, M.G., Read, R.J., Richardson, J.S., Richardson, D.C., Sammito, M.D.,

Sobolev, O.V., Stockwell, D.H., Terwilliger, T.C., Urzhumtsev, A.G., Videau, L.L., Williams, C.J., Adams, P.D., 2019. Macromolecular structure determination using X-rays, neutrons and electrons: recent developments in Phenix. Acta Crystallogr. D Struct. Biol. 75, 861–877.

Liu, W., Shi, X., Gong, P., 2018. A unique intra-molecular fidelity-modulating mechanism identified in a viral RNA-dependent RNA polymerase. Nucleic Acids Res. 46, 10840–10854.

Lu, G., Gong, P., 2013. Crystal structure of the full-length Japanese encephalitis virus NS5 reveals a conserved methyltransferase-polymerase interface. PLoS Pathog. 9, e1003549.

Maori, E., Lavi, S., Mozes-Koch, R., Gantman, Y., Peretz, Y., Edelbaum, O., Tanne, E., Sela, I., 2007. Isolation and characterization of Israeli acute paralysis virus, a dicistrovirus affecting honeybees in Israel: evidence for diversity due to intra- and inter-species recombination. J. Gen. Virol. 88, 3428–3438.

Nakashima, N., Nakamura, Y., 2008. Cleavage sites of the "P3 region" in the nonstructural polyprotein precursor of a dicistrovirus. Arch. Virol. 153, 1955–1960.

Neufeld, K.L., Richards, O.C., Ehrenfeld, E., 1991. Purification, characterization, and comparison of poliovirus RNA polymerase from native and recombinant sources. J. Biol. Chem. 266, 24212–24219.

Otwinowski, Z., Minor, W., 1997. Processing of X-ray diffraction data collected in oscillation mode. Methods Enzymol. 276, 307–326.

Paul, A.V., Wimmer, E., 2015. Initiation of protein-primed picornavirus RNA synthesis. Virus Res. 206, 12–26.

Peersen, O.B., 2019. A Comprehensive superposition of viral polymerase structures. Viruses 11.

Reddy, K.E., Noh, J.H., Kim, Y.H., Yoo, M.S., Doan, H.T.T., Ramya, M., Jung, S.C., Quyen, D.V., Kang, S.W., 2013. Analysis of the nonstructural and structural polyprotein regions, and complete genome sequences of Israel acute paralysis viruses identified from honeybees (*Apis mellifera*) in Korea. Virology 444, 211–217.

Reich, E., Franklin, R.M., Shatkin, A.J., Tatum, E.L., 1961. Effect of actinomycin D on cellular nucleic acid synthesis and virus production. Science 134, 556–557.

Shu, B., Gong, P., 2016. Structural basis of viral RNA-dependent RNA polymerase catalysis and translocation. Proc. Natl. Acad. Sci. U. S. A. 113, E4005–E4014.

Shu, B., Gong, P., 2017. The uncoupling of catalysis and translocation in the viral RNA-dependent RNA polymerase. RNA Biol. 14, 1314–1319.

Terwilliger, T.C., Adams, P.D., Read, R.J., Mccoy, A.J., Moriarty, N.W., Grosse-Kunstleve, R.W., Afonine, P.V., Zwart, P.H., Hung, L.W., 2009. Decision-making in structure solution using Bayesian estimates of map quality: the PHENIX AutoSol wizard. Acta Crystallogr. D Biol. Crystallogr. 65, 582–601.

Terwilliger, T.C., Grosse-Kunstleve, R.W., Afonine, P.V., Moriarty, N.W., Zwart, P.H., Hung, L.W., Read, R.J., Adams, P.D., 2008. Iterative model building, structure refinement and density modification with the PHENIX AutoBuild wizard. Acta Crystallogr. D Biol. Crystallogr. 64, 61–69.

Theobald, D.L., Wuttke, D.S., 2008. Accurate structural correlations from maximum likelihood superpositions. PLoS Comput. Biol. 4, e43.

Thompson, A.A., Peersen, O.B., 2004. Structural basis for proteolysis-dependent activation of the poliovirus RNA-dependent RNA polymerase. EMBO J. 23, 3462–3471.

Tong, L., Rossmann, M.G., 1997. Rotation function calculations with GLRF program. Methods Enzymol. 276, 594–611.

Vives-Adrian, L., Lujan, C., Oliva, B., Van Der Linden, L., Selisko, B., Coutard, B., Canard, B., Van Kuppeveld, F.J., Ferrer-Orta, C., Verdaguer, N., 2014. The crystal structure of a cardiovirus RNA-dependent RNA polymerase reveals an unusual conformation of the polymerase active site. J. Virol. 88, 5595–5607.

Walker, A.P., Fan, H., Keown, J.R., Knight, M.L., Grimes, J.M., Fodor, E., 2021. The SARS-CoV-2 RNA polymerase is a viral RNA capping enzyme. Nucleic Acids Res. 49, 13019–13030.

Wang, M., Li, R., Shu, B., Jing, X., Ye, H.Q., Gong, P., 2020. Stringent control of the RNA-dependent RNA polymerase translocation revealed by multiple intermediate structures. Nat. Commun. 11, 2605.

Wang, Q., Wu, J., Wang, H., Gao, Y., Liu, Q., Mu, A., Ji, W., Yan, L., Zhu, Y., Zhu, C., Fang, X., Yang, X., Huang, Y., Gao, H., Liu, F., Ge, J., Sun, Q., Yang, X., Xu, W., Liu, Z., Yang, H., Lou, Z., Jiang, B., Guddat, L.W., Gong, P., Rao, Z., 2020. Structural basis for RNA replication by the SARS-CoV-2 polymerase. Cell 182, 417–428.e13.

Wu, J., Lu, G., Zhang, B., Gong, P., 2015. Perturbation in the conserved methyltransferase-polymerase interface of flavivirus NS5 differentially affects polymerase initiation and elongation. J. Virol. 89, 249–261.

Wu, J., Wang, X., Liu, Q., Lu, G., Gong, P., 2023. Structural basis of transition from initiation to elongation in de novo viral RNA-dependent RNA polymerases. Proc. Natl. Acad. Sci. U. S. A. 120, e2211425120.

Yang, J., Jing, X., Yi, W., Li, X.D., Yao, C., Zhang, B., Zheng, Z., Wang, H., Gong, P., 2021. Crystal structure of a tick-borne flavivirus RNA-dependent RNA polymerase suggests a host adaptation hotspot in RNA viruses. Nucleic Acids Res. 49, 1567–1580.

Zhao, Y., Soh, T.S., Zheng, J., Chan, K.W., Phoo, W.W., Lee, C.C., Tay, M.Y., Swaminathan, K., Cornvik, T.C., Lim, S.P., Shi, P.Y., Lescar, J., Vasudevan, S.G., Luo, D., 2015. A crystal structure of the dengue virus NS5 protein reveals a novel inter-domain interface essential for protein flexibility and virus replication. PLoS Pathog. 11, e1004682.